GDCh Research Article Angewandte International Edition Chemie www.angewandte.org

How to cite: *Angew. Chem. Int. Ed.* **2025**, *64*, e202414524
doi.org/10.1002/anie.202414524

VIP Solid State Lithium Metal Batteries Very Important Paper

The Regulation of Solid Electrolyte Interphase on Composite Lithium Anodes in Solid-State Batteries

Zi-You Wang, Chen-Zi Zhao, Nan Yao, Yang Lu, Zhou-Qing Xue, Xue-Yan Huang, Pan Xu, Wen-Ze Huang, Zi-Xuan Wang, Jia-Qi Huang,* and Qiang Zhang*

Abstract: Solid-state lithium metal batteries (SSLMBs) with solid polymer electrolyte (SPE) are highly promising for next-generation energy storage due to their enhanced safety and energy density. However, the stability of the solid electrolyte interphase (SEI) on the lithium metal/SPE interface is a major challenge, as continuous SEI degradation and regeneration during cycling lead to capacity fading. This article investigates the SEI formation on lithium anodes (l-SEI) and composite lithium anodes (c-SEI) in solid-state lithium metal batteries. The composite anodes form a uniform Li_2S-rich inorganic SEI layer and a thinner organic SEI layer, effectively passivating the interface for enhanced cycling stability. Specifically, the full cells with c-SEI anodes sustain over 400 cycles at 0.5 C under a high areal capacity of 2.0 mAh cm^{-2}. Moreover, the reversible high-loading solid-state pouch cells exhibit exceptional safety even after curling and cutting. These findings offer valuable insights into developing composite electrodes with robust SEI for solid-state polymer-based lithium metal batteries.

Introduction

Solid-state batteries are highly regarded for their inherent safety and high energy density, making them particularly promising for various applications.[1] Solid polymer electrolytes (SPEs) offer enhanced safety and simple processing capabilities, which are also compatible with current commercial manufacturing techniques.[3] As the energy density of lithium-ion batteries (LIBs) with intercalation anodes is nearing its limit of 350 Wh kg^{-1}, the metallic lithium (Li) emerges as a highly-promising anode for SSLMBs, boasting a high theoretical specific capacity of 3860 mAh g^{-1}. Despite these advantages, challenges such as the formation of large amounts of "dead" Li and unstable SEI, particularly at high areal capacities ($\geq$2.0 mAh cm^{-2}), hinder the further development of batteries.[4] Various methods have been proposed to overcome these obstacles and extend the life of batteries, such as interface engineering,[7] electrolyte modification,[9] and employing composite Li anodes.[10]

During the past decades, the evolution and role of the SEI between the SPE and Li anode are usually overlooked. Owing to the low electrode potential of metallic Li, SPEs undergo spontaneous reductions like non-aqueous electrolytes, forming a chemically inert layer on the anode. Xin et al. employed cryo-electron microscopy to validate the presence of SEI in polymer-based solid-state battery systems.[11] The SEI undergoes continuous transformation and electrolyte consumption during cycling in SSLMBs, highlighting the importance of rational SEI stabilization design. Some efforts in molecular-level SEI design effectively prevent continuous parasitic reactions of SPE.[12] Nevertheless, constructing artificially SEI layer through electrolyte regulation often requires the introduction of electrolyte additives. The additive tends to be continuously consumed and leads to reduced safety of the SPE. Meanwhile, the evolution of the structure and components of SEI with different Li anode properties remains poorly understood in polymer-based solid-state electrolytes. The SEI structure dictates the transport rate and uniformity of Li ions (Li^+) from the electrolyte to the anode, significantly influencing the rate and polarization of electrochemical reactions at the anode/electrolyte interface.[13] The SEI in polyether electrolytes effectively prevents lithium dendrite formation and protects lithium metal, but controlling it remains crucial due to challenges like increased interface resistance and lithium-ion migration barriers.[14] Therefore, understanding the influence of the composite anode on the formation of various compounds in SEI is crucial to grasping the impact of the anode on the Li deposition kinetics.[15]

This contribution explores the evolution of SEI on metallic Li anode and composite Li anode in SSLMBs,

[*] Z.-Y. Wang, Z.-Q. Xue, Z.-X. Wang, Prof. J.-Q. Huang
School of Materials Science and Engineering
Beijing Institute of Technology
Beijing 100081 (P. R. China)
E-mail: jqhuang@bit.edu.cn

Z.-Y. Wang, Z.-Q. Xue, Z.-X. Wang, Prof. J.-Q. Huang
Advanced Research Institute of Multidisciplinary Science
Beijing Institute of Technology
Beijing 100081 (P. R. China)

Prof. C.-Z. Zhao, N. Yao, Dr. Y. Lu, Dr. X.-Y. Huang, Dr. P. Xu, Dr. W.-Z. Huang, Prof. Q. Zhang
Tsinghua Center for Green Chemical Engineering Electrification (CCEE)
Beijing Key Laboratory of Green Chemical Reaction Engineering and Technology
Department of Chemical Engineering
Tsinghua University
Beijing 100084 (P. R. China)
E-mail: zcz@mail.tsinghua.edu.cn

proposing a strategy to form a dense passivating SEI leveraging the surface advantages of composite anode electrodes. The SEI on composite anode (c-SEI) is achieved with a Li_2S-rich structure. Furthermore, we investigated how the passivation effect of c-SEI at the interface effectively inhibits the parasitic interfacial reactions of polyether by employing three-electrode techniques. The full cell with $LiFePO_4$ (LFP) cathode and c-SEI protected anode maintains over 400 cycles at 0.5 C under a high areal capacity of 2.0 mAh cm^{-2}. These findings imply that the composite anode electrode in SSLMBs can induce heterogenization of the SEI interfaces, presenting the opportunity to achieve high-performance SSLMBs through the rational design of composite Li anodes.

Results and Discussion

Microstructure of SEI on Li Metal and Composite Anodes

To directly probe the microstructure of SEI, the SEI layers of lithium metal on pure Li anode (l-SEI) and composite anode (c-SEI) were characterized by a cryo-transmission electron microscope (cryo-TEM). A double copper (Cu) mesh structure was proposed for the direct observation of the Li and SEI on the lithium anode in solid-state batteries (Figure S1), instead of routine solvent dispersion or electrochemical deposition methods.[17] Macroscopic morphology and X-ray diffraction (XRD) spectra of Cu and carbon paper (CP) are shown in Figure S2. Li plating was carried out at a consistent current density of 1.0 mA cm^{-2} for 1.0 h. Figures 1a–c display representative images of the Li and l-SEI on Cu, where noticeable Li dendrite growth occurs on the Cu surface.

The inner layer of l-SEI contains fewer inorganic compounds such as Li_2O, while the outer layer is thicker than c-SEI (Figure 1b). The uniform Li metal plating on the CP surface (Figure 1d) is advantageous for reversible deposition and stripping. Cryo-TEM images reveal a typical double-layer construction, where the c-SEI comprises a 15 nm-thick amorphous layer and an inorganic-rich layer containing Li_2S, Li_2O, and LiF (Figure 1e). The organic layer thickness in the c-SEI is reduced by around 20 %, which aids in the reduction of diffusion route length for uniform Li-ion fluxes. Corresponding selected area electron diffraction (SAED) confirms the presence of these inorganic crystalline materials and also detects diffraction rings of Li_2CO_3 and several single crystals spot patterns (Figure 1f). The c-SEI contains nanocrystals of Li_2CO_3.[18] Furthermore, the presence of single crystal spot patterns suggests the existence of a LiC_x structure, which can enhance the lithiophilic properties of c-SEI. The SAED of c-SEI layer shows significant presence of LiF, Li_2O, Li_2CO_3, and Li_2S, while the l-SEI lacks the diffraction ring corresponding to Li_2S (Figure 1c and 1f). The above results indicate that when lithium metal is deposited, the initial substrate can determine the subsequent SEI.

The EDS mapping (Figure S1) confirmed the significant quantities of oxygen, sulfur, fluorine, carbon, and nitrogen

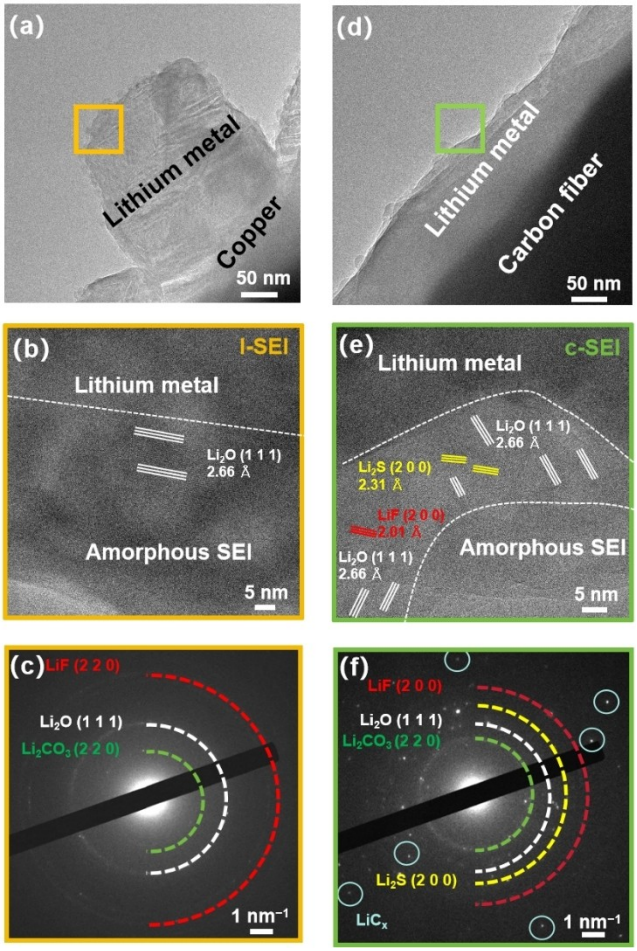

Figure 1. SEI Microstructure of l-SEI and c-SEI formed on Li metal and composite Li anode. Cryo-TEM images depict the morphology of (a) Li metal and (d) composite Li anode. The cryo-TEM images reveal the distinctive inner organic layer and outer amorphous layer of (b) l-SEI and (e) c-SEI. SAED images of the (c) l-SEI and (f) c-SEI provide further insights of components.

in c-SEI. Even in the absence of additional sulfides, the anode exhibits a significant sulfur presence (19.76 %) on the Li metal (Table S1).

To probe the composition and distribution of the SEI in three-dimensional space, time-of-flight secondary ion mass spectrometry (ToF-SIMS) was employed on cycled anodes via depth profiling. Li metal was plated and stripped five times at a constant current density of 1.0 mA cm^{-2}, maintaining a consistent deposition/stripping amount of 3.0 mAh cm^{-2}. C_2H^- is a characteristic organic component abundantly found in the SEI, and its intensity reduces with prolonged etching duration on both l-SEI and c-SEI (Figure S3a).[19] This can be attributed to the protection of polymerized 1,3-dioxolane (pDOL) organic layer on Li metal to prevent further parasitic reactions.[20] The thickness of the organic layer of c-SEI is thinner than that of l-SEI. Inorganic components such as Li_2S, Li_2O, and LiF are extensively examined in cryo-TEM, with their corresponding characteristic anion fragments selected for study ($Li_2S_2^-$, $Li_2O_2^-$, and LiF_2^-, respectively), affirming a strong valida-

tion through the results obtained from the earlier cryo-TEM analysis (Figure 1).

The 3D structure and spatial distribution of individual inorganic components on l-SEI and c-SEI are depicted in Figure 2a and 2b, respectively. The corresponding ToF-SIMS depth profiles are shown in Figure S3. The $Li_2S_2^-$ content reduces rapidly within the initial 50 s etching, with the intensity subsequently approaching 0. This observation implies that Li_2S has a minimal presence within the inner l-SEI. By comparison, the SEI formed on CP is much thinner, comprising a dense layer of organic species in the outer and an inorganic Li_2S-rich layer. The inorganic layer formed by the composite anode impedes the sustained decomposition of pDOL, thereby reducing the organic layer thickness. The distribution and gradient of LiF on the two andes are similar because of the self-sacrifice of FEC. Moreover, the inorganic

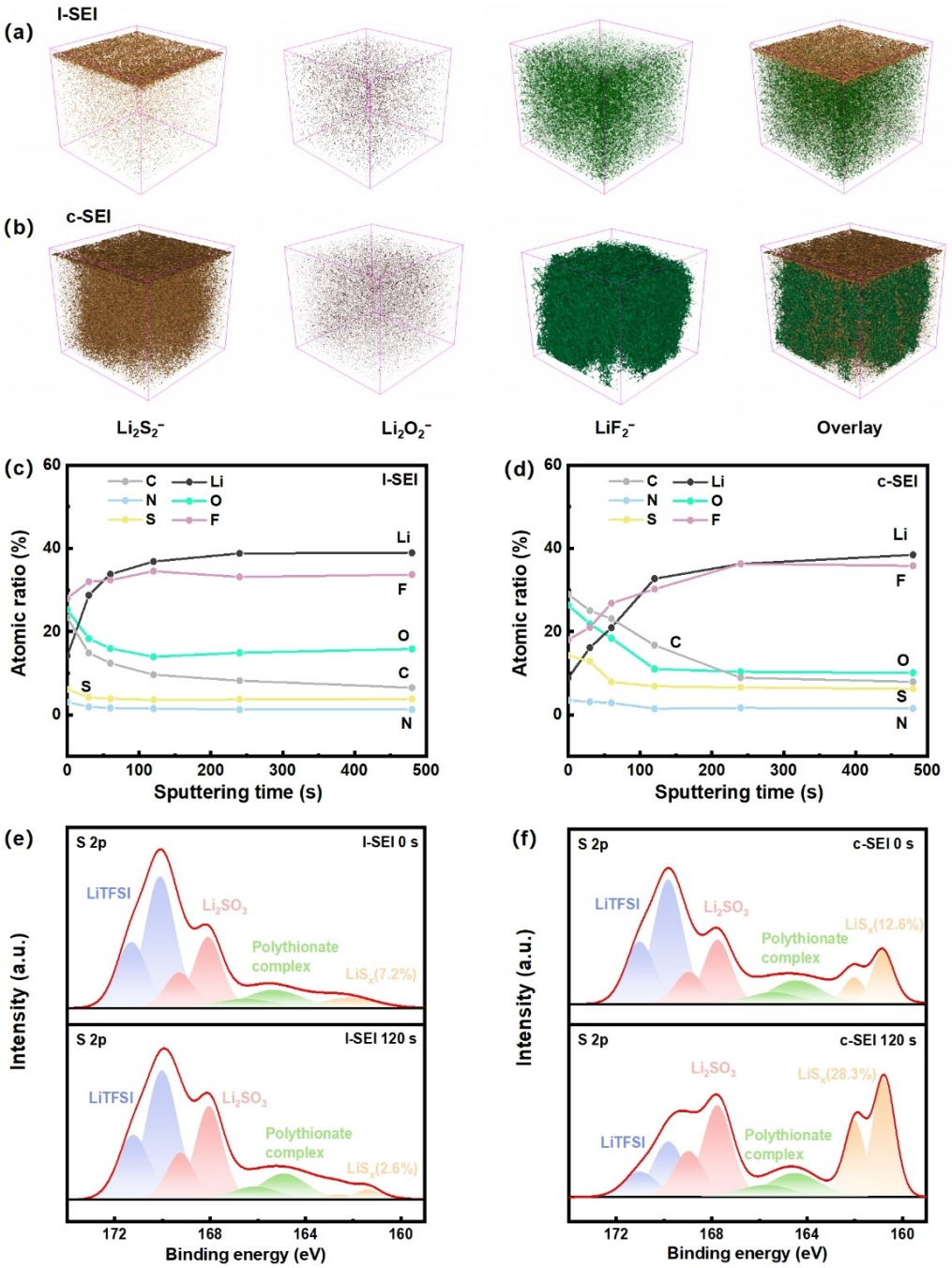

Figure 2. The 3D nanostructure of the l-SEI and c-SEI revealed through ToF-SIMS and XPS analysis. 3D views of $Li_2S_2^-$ (representing Li_2S), $Li_2O_2^-$ (representing Li_2O), LiF_2^- (representing LiF), and their overlay within the ToF-SIMS sputtered volumes of (a) l-SEI and (b) c-SEI. Additionally, the distribution of elements within the SEI formed on the (c) l-SEI and (d) c-SEI by XPS test. The XPS spectrum further demonstrates the distribution of S 2p on the (e) l-SEI and (f) c-SEI.

components of l-SEI are thinly spread in the lateral arrangement to create a dense layer. In contrast, the inorganic components on CP are closely packed, forming a sturdy layer (Figure S4).

To charactrize the SEI structure for distinct anodes, X-ray photoelectron spectroscopy (XPS) was employed for identifying the inorganic and organic components. Based on the element distribution at varying sputtering times, the composition of the SEI undergoes changes within the initial 60 s sputtering, and stabilizing after 120 s (Figure 2c and 2d). Consequently, the XPS data at 0 s and 120 s are selected for comparing the composition and content of the inner and outer layers of the SEI. Additionally, the increase in S-containing species also indicates the impact of the composite anode on electrolyte decomposition. Figure 2e and 2f illustrate the deconvoluted S 2p spectra on both the l-SEI and c-SEI, respectively. Specifically, four distinct S 2p double peaks emerge at 169.4/170.2, 167.3/168.5, 161.4/160.2, and 158.3/ 157.1, corresponding to S=O, S–O–Li, polythionate complex, and Li–S, respectively. The c-SEI exhibits a reduced presence of S=O, suggesting a heightened extent of $TFSI^-$ decomposition. Furthermore, the discernible abundance of Li_2S (28.3 % in inner layer) within the structure aligns with earlier findings from cryo-TEM and ToF-SIMS, indicating a propensity for Li_2S enrichment within the c-SEI. Furthermore, to illustrate the origin of this differentiation, the XPS results indicate that $TFSI^-$ predominantly contributes to sulfur-containing species (Figure S5). The distribution of organic components can be conveyed through the distribution of C–O species (533.5 eV) within the O 1s spectrum (Figure S6). The outer layer exhibits a notable presence of organic species for l-SEI and c-SEI (22.3 % and 29.7 %, respectively), while the inner layer exhibits minimal detection of O-containing species (12.0 % and 6.3 %, respectively) (Figure S7). Li_2S-rich inner layer structure effectively passivates the c-SEI, resulting in a lower thickness and content of organic components in the outer layer of c-SEI. In addition, the distribution of the inner and outer layers of Li_2O also exibits that the outer amorphous phase is dominated by organic species. This observation substantiates the bilayer structure of the l-SEI and c-SEI, affirming that CP does not alter the SEI structure. The distribution of Li–F and C–F in the SEI on the two anodes, as shown in the F 1s spectra, is consistent with earlier findings. By comparing the l-SEI and c-SEI without FEC, it was found that the composite anode promotes the decomposition of $TFSI^-$. This facilitates the formation of a Li_2S-rich SEI and also contributes to the generation of LiF (Figure S8). Therefore, based on the three-dimensional spatial distribution and quantitative results, the c-SEI demonstrates a significantly Li_2S-rich inorganic SEI layer. In the C 1s XPS spectra presented in Figure S9, a peak at 292.3 eV is observed in both l-SEI and c-SEI, corresponding to the $–CF_3$ functional group. This peak indicates the extent of LiTFSI decomposition and further substantiates that the decomposition of $TFSI^-$ anions is more extensive in c-SEI. Additionally, the C 1s peak at 288.4 eV, attributed to RC=OLi, is typically considered a characteristic feature of the organic SEI. The high activation energy and increased interfacial impedance associated with the R group from the long-chain pDOL contribute significantly to capacity loss and failure in SSLMBs. In c-SEI, the reduction of parasitic reactions with pDOL leads to lower quantities of RC=OLi, a result of the dense Li_2S-rich layer and the passivation effect of composite anode. Conversely, l-SEI shows more pronounced parasitic reactions and a higher content of RC=OLi.

The Formation and Evolution of SEI Layers

In the absence of additional sulfur-containing compounds, notable distinctions are observed in the S-containing species of the SEI between the two anodes. LiTFSI is a non-hydrolyzable lithium salt with strong S–C covalent bonding, suggesting that LiTFSI typically undergoes minimal decomposition into Li_2S on the lithium surface.[21] However, the c-SEI exhibits a tendency to accumulate an abundance of Li_2S. To explain the phenomenon of SEI changes, we explored variations in reaction degrees and trends across different surfaces using the electrochemistry and molecular dynamics methods. It is necessary to elucidate how S-containing species evolve and generate at the working interfaces. In the early stages of the reaction, the initial decomposition reaction of LiTFSI on Li metal is formulated as Eq. 1.[24] As Li deposition progresses, $Li_2S_2O_4$ further decomposes into lithiated compounds with smaller molecular weights (Eq. 2 and Eq. 3),[25] which can be attributed to a subsequent reduction and disproportionation of $Li_2S_2O_4$:

$$LiN(SO_2CF_3)_2 + ne^- + nLi^+ \rightarrow Li_3N + Li_2S_2O_4 + LiF + C_2F_xLi_y \quad (1)$$

$$Li_2S_2O_4 + 10e^- + 10Li^+ \rightarrow 2Li_2S + 4Li_2O \quad (2)$$

$$Li_2S_2O_4 + 4e^- + 4Li^+ \rightarrow Li_2S + Li_2SO_3 + Li_2O \quad (3)$$

Figures 3a and 3b illustrate the cyclic voltammetry (CV) curves for l-SEI and c-SEI spanning from 0 to 1 V. A distinct degradation process of LiTFSI with an initial 0.6 V cathodic peak is observeed for CP in the initial cycle. Subsequently, the disappearance of the 0.6 V cathodic peak in the second cycle suggests the formation of a stable SEI. Besides, the cathodic peaks at 0.18 and 0.07 V indicate Li intercalation processes in CP, corresponding to the formation of LiC_{12} and LiC_6, respectively. Therefore, in contrast to Cu, the use of CP enhances the reduction degrees of $TFSI^-$ anions with a large current, providing a rational explanation for the higher sulfur content in the c-SEI.[27]

In order to further clarify how the anode influences the reaction of sulfide compounds, we compute the Gibbs free energy change (ΔG) for these two reactions (Figure 3c). This calculation serves as a thermodynamic descriptor for evaluating the reaction tendency. The specific calculation models are provided in Figure S10 and S11. In this setup, the Cu potential is either set to 0 or 0.1 V, and the lithiated graphite electrode potential is fixed at 0.1 V. The calculated ΔG values are standardized by the number of electrons,

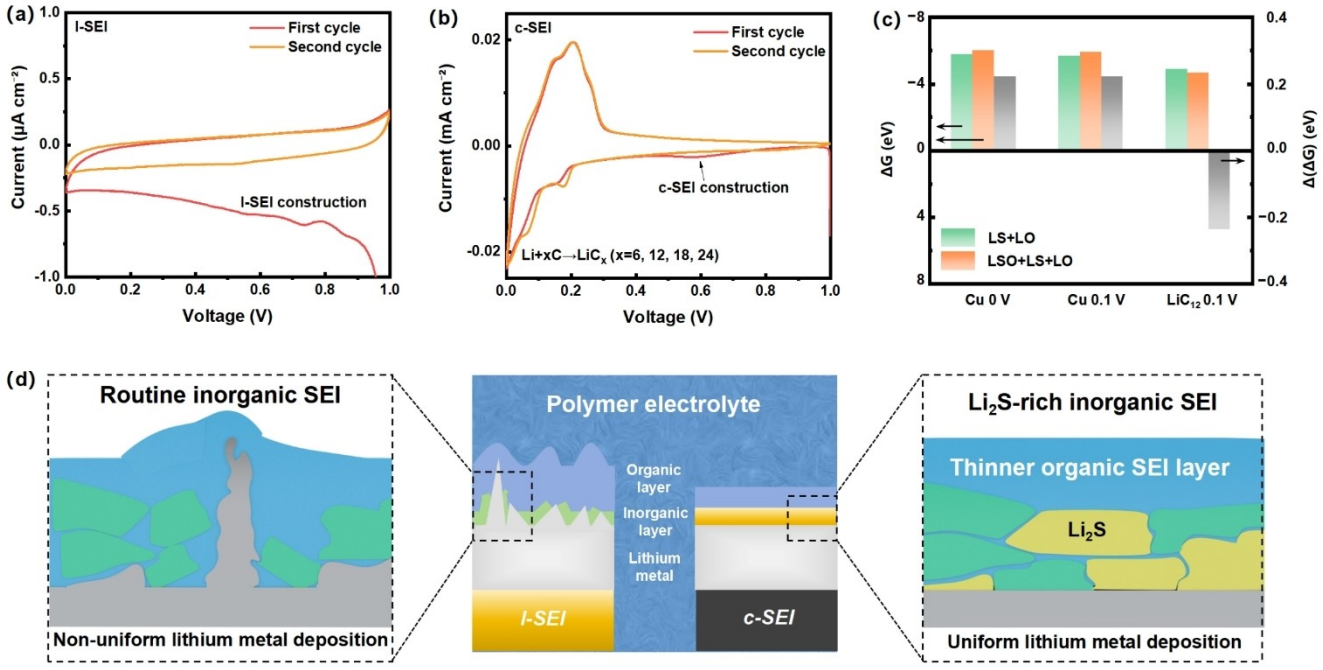

Figure 3. The Origins of Li_2S-rich inorganic SEI formation. The initial and second cycle cyclic voltammetry (CV) images depicting (a) l-SEI and (b) c-SEI. ccompanied by the outcomes of free energy calculations, ΔG_m denotes the change in free energy for the one-electron reaction involving the reduction of $TFSI^-$ to its respective products. The $\Delta(\Delta G_m)$ was calculated by subtracting ΔG_{m1} from ΔG_{m2}. (d) Schematic representation of the SEIs on routine l-SEI and c-SEI, where c-SEI demonstrates a uniform Li_2S-rich inorganic SEI layer and a thinner organic SEI layer.

resulting in the ΔG per electron transfer (ΔG_m) for the $TFSI^-$ reduction reaction. To compare the tendencies of two reactions on different anodes, we calculate the difference in ΔG_m ($\Delta(\Delta G_m) = \Delta G_{m,eq1} - \Delta G_{m,eq2}$). At both 0 and 0.1 V using the same electrode, $Li_2S_2O_4$ exhibits same reaction patterns (Both of $\Delta(\Delta G_m)$ are 0.22 eV), indicating the small potential impact on the reaction trend. However, $Li_2S_2O_4$ exhibits varying trends with different anodes at the same potential, with $\Delta(\Delta G_m)$ for LiC_{12} is −0.23 eV, in contrast to that of Cu is 0.22 eV. This illustrates that $Li_2S_2O_4$ is more inclined to reduce to inorganic Li_2S when the surface changes from l-SEI to c-SEI. The above results suggest a significant correlation between the anode type and SEI evolution. The surface of CP tends to decompose $TFSI^-$ anions, thereby generating a Li_2S-rich passivation layer. To sum up, the decomposition of $TFSI^-$ anions and the dominant inorganic species Li_2S in c-SEI contribute to constructing a stable inorganic SEI layer. This configuration significantly reduces the reactivity of the multi-electron reaction RC=OLi derived from pDOL, ultimately forming a Li_2S-rich inorganic SEI layer and a thinner organic SEI layer from pDOL (Figure S12).

Steady EIS tracked the anode|SPE interface resistances over 10 hours, revealing a growing semicircle in the chemical-formed SEI process of Li metal while Li/CP electrodes exhibit no significant changes (Figure S13). In order to accurately monitor the changes of Li deposition kinetics, impedance spectra were recorded during both the initial cycle (Figure 4a and 4b) and extended cycles (Figure 4c and 4d) in a three-electrode configuration within an in-built polymer system. A three-electrode configuration, featuring a Li@Cu reference electrode, was utilized for an accurate impedance signal measurement from the anode, effectively sidestepping issues arising with the Li counter electrode. Additionally, this configuration was carefully designed to minimize interference with ion transmission and prevent disruptions at the polymer/working electrode (WE) interface (Figure S14).

The timescale identification is a crucial method to integrate with non-destructive impedance characterizations for real-time battery monitoring.[28] The interfacial impedance evolution is tracked by utilizing a three-electrode system and the distribution of relaxation times (DRT) analysis on the electrochemical impedance spectroscopy (EIS) data. The resulting DRT plot allows for the identification of specific electrochemical processes through distinct relaxation times on the anode. The impedance is evident as a peak in the range of τ from 10^{-5} to 10^{-4} s, signifying the SEI response. Additionally, the range of τ between 0.001 and 0.01 s reflects the charge transfer resistance, while values below 0.1 s demonstrate the diffusion of Li ions. During the initial plating cycle, R_{SEI} on l-SEI possesses a larger initial value of 3.8 Ω compared to 1.5 Ω for c-SEI, and occupies the main part of the impedance (53.3 %), indicating uneven SEI growth (Figure 4a). Hence, the non-uniform plating-stripping mechanism generates additional SEI throughout cycling, leading to a continuous increase in R_{SEI}. However, c-SEI exhibits stable R_{SEI} (1.5 Ω) in the whole timescale identification during the first deposition process with a high Li stripping capacity (Fig-

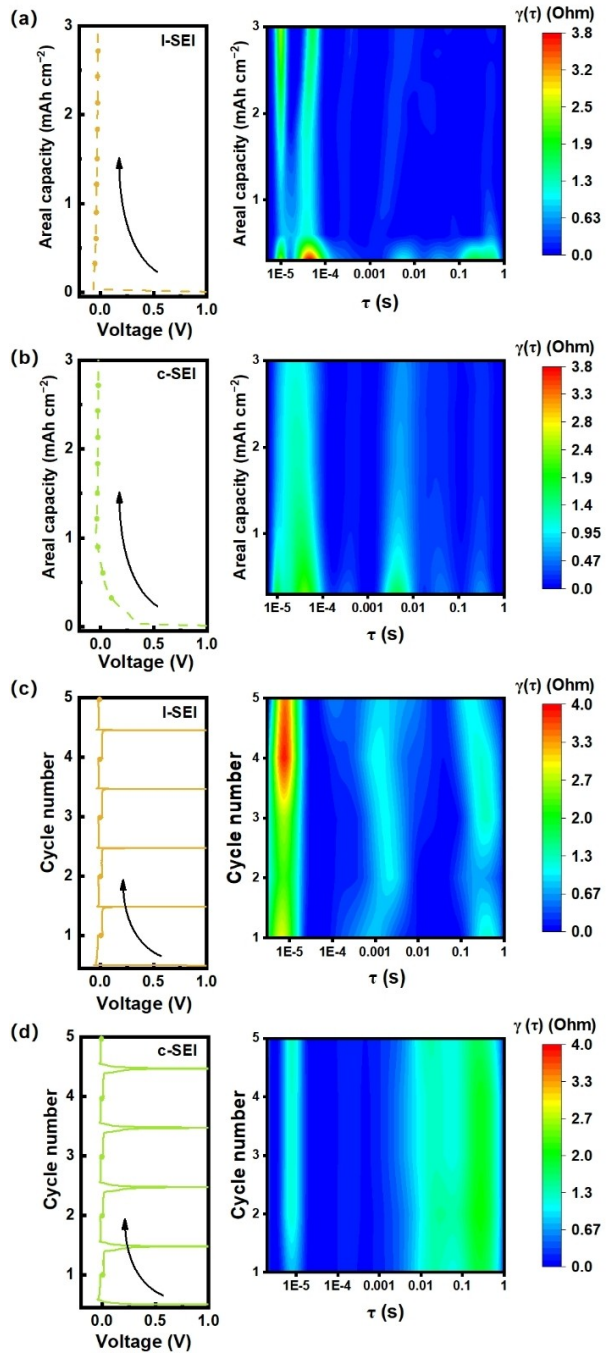

Figure 4. DRT transition analysis of three-electrode EIS evaluation for SSLMB during Li plating and stripping. Figure (a) and (b) present initial deposition and impedance time distribution o Li anode and composite anode, respectively. Furthermore, it provides voltage-cycle curve for 5 cycles and DRT analysis of (c) Li anode and (d) composite Li anode, respectively. All cycles were consistently executed at 3.0 mAh cm^{-2} and 1.0 mA cm^{-2}.

ure 4b). The Li metal can maintain stable growth, avoiding the inhomogeneous interfacial Li^+ flux derived from an uneven SEI. Throughout the cycling process, the R_{SEI} on l-SEI exhibits a notable increase, contrasting with the stable state of c-SEI (Figure 4d and 4e). The activation energy of the SEI was determined using temperature-dependent EIS measurements (Figure S15). Following the deposition of 0.3 mAh cm^{-2} and 5 cycles, the activation energy of the c-SEI (0.72 and 0.69 eV, respectively) is observed to be lower than that of l-SEI (0.89 and 0.84 eV, respectively). This suggests that Li^+ encounters less hindrance when passing through the c-SEI. However, Zaban and colleagues speculate that it requires a range of 0.30 to 0.83 eV per atom for Li^+ to move in the SEI formed in different electrolytes.[29] The increased activation energy in SPE systems, linked to SEI composition variations, emphasizes challenges in controlling Li deposition kinetics in polymer electrolytes and underscores the critical role of SEI.[30] The enhanced Li deposition kinetics can be attributed to the large amount of Li_2S within the interfacial layer. Despite the inherent low Li ion conductivity of bulk Li_2S at room temperature, the nanoscale Li_2S-rich SEI demonstrates notable improvement in Li ion conductivity and reduced interfacial activation energy.[31]

Additionally, testing at different current densities demonstrates the anode's excellent lithiophilicity (Figure S16). The c-SEI anode exhibits a lower nucleation overpotential and a higher exchange current density, indicating improved Li^+ transfer with c-SEI. To further verify the effect of l-SEI and c-SEI on lithium metal deposition kinetics, the Coulombic efficiencies of half-cell batteries with Cu and CP were examined under a consistent current density of 1.0 mA cm^{-2} and an areal capacity of 1.0 and 3.0 mAh cm^{-2} (Figure S17). Coulombic efficiency of Cu unexpectedly drops in the 30th cycle due to continuous electrolyte consumption and accumulation of dead Li metal. Conversely, half-cells employing CP consistently maintain a stable Coulombic efficiency (> 98.5 %) after 120th cycles. The Li_2S passivation layer effectively inhibits the further degradation of $TFSI^-$ anion and pDOL, resulting in high Coulombic efficiency and longer cycle life. SEM images reveal distinct Li deposition patterns under the two SEIs. Figure S18 shows that c-SEI leads to denser Li deposits, while l-SEI results in uneven deposition. After 10 mAh cm^{-2}, c-SEI forms a compact structure with less volume expansion, highlighting its superior performance (Figure S19). The composite lithium anode is created by directly rolling ultrathin Li foils onto carbon paper host/planar Cu foil at room temperature (Figure 5a). The subsequent in situ polymerization process for creating integrated composite anodes facilitates large-scale production. Li plating/stripping experiments were conducted in Li anode with normal l-SEI anode|SPEs|l-SEI anode and c-SEI anode|SPEs|c-SEI anode symmetrical cell configurations to investigate the cycling reversibility of two anodes (Figure S20). As shown in Figure S20c, during the initial 10 to 20 h, c-SEI anode exhibits smaller polarization, with no notable concentration polarization peak or micro-Li-bulk Li transition peak observed. This is attributed to the superior deposition kinetics of c-SEI anode and a small occurrence of dead Li. When the duration is extended to 130 h, the c-SEI anode consistently maintains low polarization of 20 mV, in contrast to Li, which exhibits a polarization close to 50 mV. The increase of voltage signals the heightened challenge in initiating Li nucleation during the plating and stripping

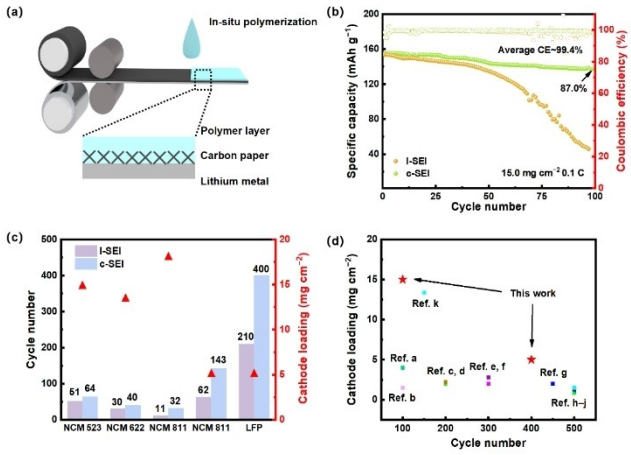

Figure 5. Electrochemical performances of l-SEI and c-SEI anodes. (a) Schematic representation of the c-SEI anode fabrication process utilizing the rolling method. (b) The long-term cycling performance for the 15.0 mg cm^{-2} LFP electrode. (c) Long-term cycling performance with different cathodes and corresponding areal loading. (d) The comparison of cathode material loading and cycle number for the SSLMBs.[32]

during the reversing phase of the cycle. This phenomenon is typically linked to the development of a substantial SEI at the electrode and the buildup of electronically isolated or dead Li at the working interfaces. When the accumulation of dead Li and the SEI with electronic insulation reaches a critical point, polarization sharply increases, ultimately resulting in the failure of the Li–Li symmetrical battery after 350 h. These findings indicate that c-SEI effectively suppresses undesirable reactions between Li and the electrolyte, ensuring sustained high reversibility during repeated Li plating/stripping.

Practical Applications of C-SEI Composite Anodes

The c-SEI composite anodes are applied in both coin-type and pouch-type full cells. The specific capacity of $LiFePO_4$ (LFP)|l-SEI anode sharply reduces to 93.8 mAh g^{-1} after 200 cycles in coin cells (Figure S21), mainly attributed to the formation of a thick layer of "dead" Li and SEI (Figure S22). In contrast, the LFP|c-SEI anode configuration demonstrates a higher specific capacity compared to a standard LFP|l-SEI anode cell. The LFP|c-SEI anode consistently maintains a specific capacity of 122.5 mAh g^{-1} through 400 cycles at 0.5 C. The LFP|c-SEI anode cell demonstrates improved specific capacities under various rates (Figure S23). Upon reverting to a 0.2 C rate, the LFP|c-SEI anode impressively retains 98.0 % of its initial capacity, demonstrating remarkable stability. In contrast, the LFP|l-SEI anode experiences a noticeable decline to about 85.4 % in capacity retention, indicating the inherent instability in the charging and discharging processes and inferior reversibility of Li anodes. When the c-SEI anodes are paired with high-loading cathodes (15.0 mg cm^{-2}), the full cells can still maintain a high capacity and a long lifespan. The high-loading LFP full cell with bare metallic Li exhibits rapid capacity fading over 60 cycles (Figure 5b), which is attributed to slow Li deposition kinetics at higher capacities and resulting in increased dead lithium and SEI accumulation. After 60 cycles, the routine battery exhibits a notable rise in polarization, accompanied by a rapid capacity decline (less than 80 % of the initial capacity) (Figure S24). Nevertheless, the high-loading LFP|c-SEI anode battery demonstrates impressive capacity retention, maintaining 87.0 % of its initial discharge capacity (132.1 mAh g^{-1}). The integration of constructing and stabilizing a consistent Li^+ transport pathway enhances the uniform distribution of Li^+ ions flux.

The c-SEI anode achieves an impressive improvement in cycle life compared to l-SEI anodes when matched with different types and loadings of NCM cathodes (Figure 5c and S22). The fast capacity fading is attributed to the intrinsic instability of pDOL at high voltage, yet it still highlights the potential for advancing high-energy-density SSLMBs. The c-SEI anodes show excellent electrochemical performance in SSLMBs, and a comparison of cathode material loading and cycle number of the current works related to the SSLMBs was illustrated in Figure 5d, S25 and Table S2. As shown above, we achieved more significant progress in areal loading and cycling lifetime, which can be attributed to the regulation of the solid electrolyte interphase on composite lithium anodes. A high energy density LFP full cell with Li anodes and polymer electrolytes is therefore achieved. Moreover, we create a prototype cathode-supported LFP-based pouch cell and it exhibits a satisfactory discharge capacity of 149.3 mAh g^{-1} at 0.1 C at 25 °C (Figure S26). The safety performance of the pouch cell is further assessed using bending and corner-cut tests. The cell can operate steadily in various situations without safety issues, demonstrating the intrinsic safety performance of polymer lithium metal batteries and their potential for practical application.

Conclusions

The composite electrode surface significantly regulates the formation of SEI layer in SSLMBs. The composition of the anode influences the ΔG_m for reducing SPEs, which affects the SEI layer's composition. Specifically, the composite electrode surface promotes the decomposition of LiTFSI into a Li_2S-rich inorganic SEI layer and pDOL into a thin organic SEI layer. Employing this additive-free strategy, we have successfully obtained a Li_2S-rich SEI layer, serving as a passivation layer on anode/SPE surfaces. An improved Coulombic efficiency (>98.5 %) at high areal capacity (3.0 mAh cm^{-2}) and extended cycle life were achieved. Specially, the composite anode crafted through a straightforward one-step method has been effectively employed in practical applications. The full cells also demonstrate impressive long-term cycling stability and maintain a consistent specific capacity of 122.5 mAh g^{-1} over 400 cycles at 0.5 C. Furthermore, the composite anodes exhibit an excellent reversibility and safety in solid-state pouch cells

when paired with high-loading cathodes exceeding 15.0 mg cm^{-2} under various conditions. This contribution affords valuable insights into the structural evolution of the SEI, emphasizing the pivotal influence of the anode material on SEI formation in working SSLMBs.

Acknowledgements

This work was supported by Beijing Natural Science Foundation (Z200011, L233004), the National Key Research and Development Program (2021YFB2500300) and the National Natural Science Foundation of China (52394170, 52394171, 22393900, and 22108151).

Conflict of Interest

The authors declare no conflict of interest.

Data Availability Statement

The data that support the findings of this study are available from the corresponding author upon reasonable request.

Keywords: composite electrodes · lithium metal anodes · solid polymer electrolytes · solid electrolyte interphases · solid-state lithium metal batteries

[1] Q. Zhao, S. Stalin, C.-Z. Zhao, L. A. Archer, *Nat. Rev. Mater.* **2020**, *5*, 229–252.
[2] K. Yoon, S. Lee, K. Oh, K. Kang, *Adv. Mater.* **2022**, *34*, 2104666.
[3] D. Zhang, S. Li, Q. Xiong, Z. Huang, H. Hong, S. Yang, J. Zhu, C. Zhi, *MetalMat* **2024**, e13.
[4] P. Shi, T. Li, R. Zhang, X. Shen, X. B. Cheng, R. Xu, J. Q. Huang, X. R. Chen, H. Liu, Q. Zhang, *Adv. Mater.* **2019**, *31*, 1807131.
[5] J. Liu, H. Yuan, H. Liu, C. Z. Zhao, Y. Lu, X. B. Cheng, J. Q. Huang, Q. Zhang, *Adv. Energy Mater.* **2022**, *12*, 2100748.
[6] S. J. Yang, F. N. Jiang, J. K. Hu, H. Yuan, X. B. Cheng, S. Kaskel, Q. Zhang, J. Q. Huang, *Electron* **2023**, *1*, e8.
[7] P. Ding, Z. Lin, X. Guo, L. Wu, Y. Wang, H. Guo, L. Li, H. Yu, *Mater. Today* **2021**, *51*, 449–474.
[8] L. Wang, J. Wu, C. Bao, Z. You, Y. Lu, Z. Wen, *SusMat* **2024**, *4*, 72–105.
[9] S. Choudhury, S. Stalin, D. Vu, A. Warren, Y. Deng, P. Biswal, L. A. Archer, *Nat. Commun.* **2019**, *10*, 4398.
[10] P. Shi, X. Q. Zhang, X. Shen, R. Zhang, H. Liu, Q. Zhang, *Adv. Mater. Technol.* **2020**, *5*, 1900806.
[11] R. Lin, Y. He, C. Wang, P. Zou, E. Hu, X.-Q. Yang, K. Xu, H. L. Xin, *Nat. Nanotechnol.* **2022**, *17*, 768–776.
[12] Y. Gao, Z. Yan, J. L. Gray, X. He, D. Wang, T. Chen, Q. Huang, Y. C. Li, H. Wang, S. H. Kim, *Nat. Mater.* **2019**, *18*, 384–389.
[13] P. Zhai, L. Liu, X. Gu, T. Wang, Y. Gong, *Adv. Energy Mater.* **2020**, *10*, 2001257.
[14] C. Yang, K. Fu, Y. Zhang, E. Hitz, L. Hu, *Adv. Mater.* **2017**, *29*, 1701169.
[15] X. B. Cheng, R. Zhang, C. Z. Zhao, F. Wei, J. G. Zhang, Q. Zhang, *Adv. Sci.* **2016**, *3*, 1500213.
[16] W. Tang, N. Shen, X. Xiong, H. Liu, X. Sun, J. Guo, F. Jiang, T. Wang, Y. Ma, Y. Zhong, *Energy Mater. Adv.* **2024**, *5*, 0084.
[17] J. Wang, W. Huang, A. Pei, Y. Li, F. Shi, X. Yu, Y. Cui, *Nat. Energy* **2019**, *4*, 664–670.
[18] S. Y. Sun, N. Yao, C. B. Jin, J. Xie, X. Y. Li, M. Y. Zhou, X. Chen, B. Q. Li, X. Q. Zhang, Q. Zhang, *Angew. Chem. Int. Ed.* **2022**, *61*, e202208743.
[19] J. Wu, Z. Gao, Y. Tian, Y. Zhao, Y. Lin, K. Wang, H. Guo, Y. Pan, X. Wang, F. Kang, *Adv. Mater.* **2023**, *35*, 2303347.
[20] L.-x. Li, R. Li, Z.-h. Huang, H. Yang, M.-q. Liu, J. Xiang, S. Hussain, X.-q. Shen, M.-x. Jing, *ACS Appl. Mater. Interfaces* **2022**, *14*, 30786–30795.
[21] C. Lai, C. Shu, W. Li, L. Wang, X. Wang, T. Zhang, X. Yin, I. Ahmad, M. Li, X. Tian, *Nano Lett.* **2020**, *20*, 8273–8281.
[22] C.-Z. Zhao, X.-B. Cheng, R. Zhang, H.-J. Peng, J.-Q. Huang, R. Ran, Z.-H. Huang, F. Wei, Q. Zhang, *Energy Storage Mater.* **2016**, *3*, 77–84.
[23] B. N. Olana, S.-H. Pan, B.-J. Hwang, H. Althues, J.-C. Jiang, S. D. Lin, *J. Mater. Chem. A* **2024**, *12*, 3659–3670.
[24] J. Li, H. Hu, W. Fang, J. Ding, D. Yuan, S. Luo, H. Zhang, X. Ji, *Adv. Funct. Mater.* **2023**, 2303718.
[25] V. Aravindan, J. Gnanaraj, S. Madhavi, H. K. Liu, *Chem. Eur. J.* **2011**, *17*, 14326–14346.
[26] C. Xu, B. Sun, T. Gustafsson, K. Edström, D. Brandell, M. Hahlin, *J. Mater. Chem. A* **2014**, *2*, 7256–7264.
[27] M. Tułodziecki, J.-M. Tarascon, P.-L. Taberna, C. Guéry, *Electrochem. Commun.* **2017**, *77*, 128–132.
[28] Y. Lu, C.-Z. Zhao, J.-Q. Huang, Q. Zhang, *Joule* **2022**, *6*, 1172–1198.
[29] A. Zaban, E. Zinigrad, D. Aurbach, *J. Phys. Chem.* **1996**, *100*, 3089–3101.
[30] M. Steinhauer, S. Risse, N. Wagner, K. A. Friedrich, *Electrochim. Acta* **2017**, *228*, 652–658.
[31] X.-B. Cheng, C. Yan, H.-J. Peng, J.-Q. Huang, S.-T. Yang, Q. Zhang, *Energy Storage Mater.* **2018**, *10*, 199–205.
[32] R. Fang, B. Xu, N. S. Grundish, Y. Xia, Y. Li, C. Lu, Y. Liu, N. Wu, J. B. Goodenough, *Angew. Chem. Int. Ed.* **2021**, *133*, 17842–17847.
[33] X. Fu, C. Shang, M. Yang, E. M. Akinoglu, X. Wang, G. Zhou, *J. Power Sources* **2020**, *475*, 228687.
[34] D. Chen, M. Zhu, P. Kang, T. Zhu, H. Yuan, J. Lan, X. Yang, G. Sui, *Adv. Sci.* **2022**, *9*, 2103663.
[35] Y. Wang, R. Xu, B. Xiao, D. Lv, Y. Peng, Y. Zheng, Y. Shen, J. Chai, X. Lei, S. Luo, *Mater. Today Phys.* **2022**, *22*, 100620.
[36] Z. Li, W. Tang, Y. Deng, M. Zhou, X. Wang, R. Liu, C.-a. Wang, *J. Mater. Chem. A* **2022**, *10*, 23047–23057.
[37] S. Zeng, G. M. Arumugam, W. Li, X. Liu, X. Li, H. Zhong, F. Guo, Y. Mai, *J. Energy Chem.* **2020**, *51*, 222–229.
[38] J. Wen, Q. Zhao, X. Jiang, G. Ji, R. Wang, G. Lu, J. Long, N. Hu, C. Xu, *ACS Appl. Energ. Mater.* **2021**, *4*, 3660–3669.
[39] J. Jie, Y. Liu, L. Cong, B. Zhang, W. Lu, X. Zhang, J. Liu, H. Xie, L. Sun, *J. Energy Chem.* **2020**, *49*, 80–88.
[40] Y. Liu, Y. Xu, *Chem. Eng. J.* **2022**, *433*, 134471.
[41] H. Xu, J. Zhang, H. Zhang, J. Long, L. Xu, L. Mai, *Adv. Energy Mater.* **2023**, *13*, 2204411.
[42] T. Chen, H. Wu, J. Wan, M. Li, Y. Zhang, L. Sun, Y. Liu, L. Chen, R. Wen, C. Wang, *J. Energy Chem.* **2021**, *62*, 172–178.

Manuscript received: July 31, 2024
Accepted manuscript online: October 9, 2024
Version of record online: November 12, 2024